INTERNATIONAL JOURNAL FOR NUMERICAL METHODS IN BIOMEDICAL ENGINEERING
Int. J. Numer. Meth. Biomed. Engng. 2012; **28**:3–24
Published online 17 October 2011 in Wiley Online Library (wileyonlinelibrary.com). DOI: 10.1002/cnm.1467

Numerical simulation of a thermodynamically consistent four-species tumor growth model

Andrea Hawkins-Daarud, Kristoffer G. van der Zee and J. Tinsley Oden*,†

Institute for Computational Engineering and Sciences, The University of Texas at Austin, 1 University Station C0200, Austin, TX 78712, USA

SUMMARY

In this paper, we develop a thermodynamically consistent four-species model of tumor growth on the basis of the continuum theory of mixtures. Unique to this model is the incorporation of nutrient within the mixture as opposed to being modeled with an auxiliary reaction-diffusion equation. The formulation involves systems of highly nonlinear partial differential equations of surface effects through diffuse-interface models. A mixed finite element spatial discretization is developed and implemented to provide numerical results demonstrating the range of solutions this model can produce. A time-stepping algorithm is then presented for this system, which is shown to be first order accurate and energy gradient stable. The results of an array of numerical experiments are presented, which demonstrate a wide range of solutions produced by various choices of model parameters. Copyright © 2011 John Wiley & Sons, Ltd.

Received 20 April 2011; Revised 19 July 2011; Accepted 25 July 2011

KEY WORDS: tumor growth; mixture theory; gradient stable

1. INTRODUCTION

Computational models of tumor growth are gradually becoming an accepted mode of investigating the behavior and the response of tumors to various environment conditions and possible treatments. The idea that such a model could predict, even qualitatively, the emergence, growth, or decline of tumors in living tissue is enormously intriguing. With such a tool, researchers could, for instance, perform initial studies of treatment paradigms on computational tumors instead of tumors implanted in animals or identify prominent environmental factors that may be treatment targets. It is possible that if brought to a high enough level of sophistication, this kind of technology could revolutionize medicine and bring a new paradigm into the treatment and prevention of a class of the deadliest maladies affecting humankind. In principle, there is nothing about the classical scientific method that suggests that this is an impossible goal, and the growing literature on tumor modeling over the past decade attests that a significant progress has been made in this direction.

Work directed at mathematical modeling of tumor growth can be found in the literature throughout the last century, but only recently have the models shifted focus from mimicking growth rates from nutrient diffusion in avascular tumors to monitoring changes in tumor behavior resulting from more complex phenomena. That is, although tumor growth is now understood to be a multiscale modeling phenomena, early experiments were only able to capture and interpret events happening on a single macroscale. Because of the many advances in experimental techniques and methods developed in the early 1980s through today, such as, polymerase chain reaction [1], many discoveries have been made concerning mechanisms now known to be critical to tumor growth, including

*Correspondence to: J. Tinsley Oden, Institute for Computational Engineering and Sciences, The University of Texas at Austin, 1 University Station C0200, Austin, TX 78712, USA.

†E-mail: oden@ices.utexas.edu

the six hallmarks of cancer [2] such as angiogenesis, cell movement, and cell mutations. In turn, the number of mathematical models of tumor growth has dramatically increased along with the general level of complexity. A comprehensive history has been compiled by Araujo and McElwain [3] in 2004, and several surveys of models have also appeared in more recent years, that is, those compiled in Wodarz and Komarova [4], Bellomo *et al*. [5, 6], Preziosi [7], Lowengrub *et al*. [8], and many others [9–21]. These indicate that the majority of models can be placed into one of three categories: discrete models, also known as cellular automata models; continuum models, which are the focus of this paper; and hybrid models utilizing elements of both discrete and continuum models.

The continuum theory of mixtures, which is discussed at length in later parts of this paper, provides a mathematical framework for incorporating multiple phases within a single model. The framework for the continuum theory of mixtures was pioneered in the 1960s and 1970s by Truesdell and Toupin [22] and Bowen [23], and by the mid-1990s, it was regarded as a fairly mature theory for describing non-biologically growing media. It was not until the late 1990s that applications to biological growth began to appear in the literature. The first such model was presented by Please *et al*. in 1998 [24] exploring, in one dimension, the possible formation of a necrotic core due to stress within the tumor in the context of two phases: tumor cells, assumed inviscid, and extracellular water. Shortly afterward, this model was extended to three dimensions and included surface tension [25]. A different approach was used by Breward *et al*. [26], who assumed the existence of an inviscid aqueous phase but allowed the viscosity of the tumor cells to vary as a function of their level of differentiation, higher differentiation corresponding to higher viscosity. This approach was an attempt to simulate the cell–cell interactions that form between cells. Two other models were proposed by Preziosi and Farina [27] and Araujo and McElwain [28] in which a solid matrix was considered to be present among the other two phases, in the spirit of porous media. These models have been extended to include the host tissue as a third phase [29–31] and to begin considering multiscale adhesion effects resulting from surface molecules attaching to the extracellular matrix [32]. A one-dimensional three-phase model investigating vascular tumor growth has also been considered in this framework by Breward *et al*. [33], including blood vessels as a third phase. Other models have studied residual stress and interstitial fluid pressure aspects of the tumor tissue especially in regard to vascular collapse [34–37]. These models were influenced by many experiments showing that pressure and stress values were different in tumorous and healthy tissue and that vascular collapse was non-uniformly present throughout the tumor, implying the presence of residual stresses [38–40]. Recently, there has been a four-phase model proposed by Wise *et al*., the derivation of which is discussed at length in the papers [41–45]. This model considers tumor live cells, tumor dead cells, host cells, and an extracellular fluid, in contrast to the other mixture models under the influence of a convective velocity. The chosen form of the free energy leads to a diffuse-interface model of Cahn–Hilliard type. The simulations resulting from these equations have shown impressive qualitative agreement with brain tumor images. This group has also developed a two-phase diffuse-interface model of tumor growth including a chemotaxis term in the free energy [46].

Each of these models include the effects of some form of nutrient, say oxygen, to drive the tumor growth. Generally, because of the discrepancy in size, this species is not considered as a component in the mixture subject to the constraints given by the mixture framework. Rather, it has been dealt with using an auxiliary reaction-diffusion type equation. In this paper, we present a four-species model that incorporates the nutrient within the mixture. This has several advantages. Firstly, it provides a more consistent approach as all of the equations are considered when deriving constraints from the second law of thermodynamics. Secondly, this model can be categorized as a dissipative gradient flow, meaning that the total free energy decreases with every time step. This fact leads to the development of a gradient stable, first-order accurate, linear time-stepping scheme, which is then coupled with a mixed finite element spatial discretization to solve the system of governing equations. A general weak mixed variational statement for this class of problems is developed and used as a basis for a class of mixed finite element models.

This paper is organized as follows. Following this introduction, the general continuum theory of mixtures is briefly presented in Section 2, after which the assumptions and simplifications leading to our four-species model are discussed at length in Section 3. The idea and development of a gradient-stable time-stepping algorithm for the model is then presented in Section 4. This scheme is shown to

DOI: 10.1002/cnm

be first order accurate, gradient stable, and mass conserving. In Section 5, numerical examples are given showing the wide range of results that can be produced with this model along with numerical evidence of the theoretical results shown in Section 4.

2. THE CONTINUUM THEORY OF MIXTURES

The fundamental idea underlying mixture theory is that a material body $\mathcal{B}$ can be composed of N constituent species $\mathcal{B}_1, \ldots, \mathcal{B}_N$. These occupy a common portion of space at the same time. Each spatial position is then allowed to be occupied by N constituents, and each constituent is assigned a mass density $\hat{\rho}_\alpha$, regarded as a function of position and time, $(\mathbf{x}, t)$, which represents the mass of the αth constituent per unit volume of the mixture.

Each of the N constituents must satisfy its own balance laws, which differ from those of classical continuum mechanics because of the presence of interaction terms representing the exchange of mass, momentum, and energy between constituents. In this paper, we focus on the principal mechanisms of mass exchange and conservation of mass among species, ignoring momentum and energy transfer for simplicity.

For a general mixture occupying an open region Ω in $\mathbb{R}^3$ over a time interval $(0, T)$, the volume fractions, φ_α, and other independent field variables must satisfy the following mass balance law for all α, $1 \leqslant \alpha \leqslant N$, all $\mathbf{x} \in \Omega$, and $t \in (0, T)$.

$$\frac{\partial \rho_\alpha \varphi_\alpha}{\partial t} + \nabla \cdot (\rho_\alpha \varphi_\alpha \mathbf{v}_\alpha) = \gamma_\alpha - \nabla \cdot \mathbf{j}_\alpha. \tag{1}$$

In (1), ρ_α is the mass density per unit volume of constituent of the αth constituent, γ_α is the mass supplied to constituent α by other constituents, $\mathbf{j}_\alpha$ is the mass flux due to changes in the chemical potential defined in terms of gradients in concentrations and changes in nutrient concentrations, and $\mathbf{v}_\alpha$ is the species velocity field. These effects were introduced in the models of Cristini *et al*. [46], Frieboes *et al*. [42], and Wise *et al*. [44]. For the general theory, see [47].

Equation (1) is closed by the appropriate choices of constitutive equations, which must be consistent with both the second law of thermodynamics for the mixture and the classical balance laws for the entire mixture. By introducing the Helmholtz free energy per unit mass ψ_α for each constituent, or the free energy Ψ_α per unit volume, the classical Coleman–Noll method makes use of the constraints from classical balance laws and the second law to supply sufficient conditions on forms of key constitutive equations in terms of appropriate derivatives of the free energy [46–48]. In this work, we confine our attention to materials for which the Helmholtz free energy is of the form $\Psi_\alpha = \Psi_\alpha(\varphi_1, \ldots, \varphi_N, \nabla\varphi_1, \ldots, \nabla\varphi_N, m_1, \ldots, m_L)$. The values m_l, $1 \leqslant l \leqslant L$, here represent concentrations of chemicals or small polypeptides, which interact with the species ϕ_α but are so much smaller in size than the constituents that it is not necessary to consider them directly within the mixture, for example, oxygen or glucose. We note that it can be argued that resulting consistent constitutive equations for $\mathbf{j}_\alpha$ are of the form, $1 \leqslant \alpha \leqslant N$,

$$\mathbf{j}_\alpha = -\sum_{\beta=1}^{N} M_{\alpha\beta}(\boldsymbol{\varphi}, \mathbf{m}_\alpha) \nabla(\mu_{\beta\alpha}/\rho_\alpha), \tag{2}$$

where $M_{\alpha\beta}$ is a positive semi-definite, second-order mobility tensor and $\mu_{\beta\alpha}$ is interpreted as the chemical potential, defined as

$$\mu_{\beta\alpha} = \frac{\partial \Psi_\beta}{\partial \varphi_\alpha} - \nabla \cdot \frac{\partial \Psi_\beta}{\partial \nabla \varphi_\alpha}. \tag{3}$$

Other details on this theory are given in [47].

DOI: 10.1002/cnm

3. FOUR-SPECIES MIXTURE

A four-species model is reduced from the general framework with a species representing the tumor cell concentration and the healthy cell concentration along with two species identified with extracellular water. A departure from the previous derivations in the literature is that the extracellular water is divided into two species, one which is nutrient rich and the other which is nutrient poor. In this way, the nutrient is assumed to evolve within the extracellular water but may have different concentrations throughout. Thus, the mixture is composed of the following four species:

- $\varphi_1 = u :=$ tumor cell volume fraction,
- $\varphi_2 = h :=$ healthy cell volume fraction,
- $\varphi_3 = n :=$ nutrient-rich extracellular water volume fraction,
- $\varphi_4 = w :=$ nutrient-poor extracellular water volume fraction.

Such a mixture is illustrated in Figure 1.

The mixture is assumed to be saturated; that is, $u + h + n + w = 1$ everywhere. However, two additional constraints are imposed: the total concentration of cells remains constant throughout the domain, that is, $u + h = C$ everywhere; and, because of the first saturation constraint, the total concentration of extracellular water remains constant, that is, $n + w = 1 - C$ everywhere. The constants C and $1 - C$ can be rescaled to be unity so that the values of u and h as well as n and w are normalized so as to take on values between 0 and 1.

Next, the Helmholtz free energy must be specified for the system. In general, the tumor cells remain segregated from the healthy cells, so that the two species are similar to the species of the classical Cahn–Hilliard free energy. However, such a stark separation between the two water species is not anticipated, and thus, neither a surface energy nor a double well potential with respect to the nutrient rich extracellular water terms is included in the free energy. We assume that the presence of the nutrient-rich extracellular water increases the amount of energy which is ultimately in the system, characterized with a term n^2 in the free energy. In this manner, without interaction, the dynamics of the nutrient species is simply governed by diffusion. Finally, a term is included in the energy functional which attains a minimum when there is a full interaction between the tumor species and the nutrient-rich extracellular water; that is, this term will be minimized when both $u = 1$ and $n = 1$. This term ultimately drives the tumor cells to move toward the oxygen supply, as expected for such biological systems. From all these considerations, the total free energy of the system can be written as follows:

$$E = \int_\Omega \left(f(u) + \frac{\epsilon^2}{2} |\nabla u|^2 + \chi(u,n) + \frac{1}{2\delta} n^2 \right) \mathrm{d}x. \tag{4}$$

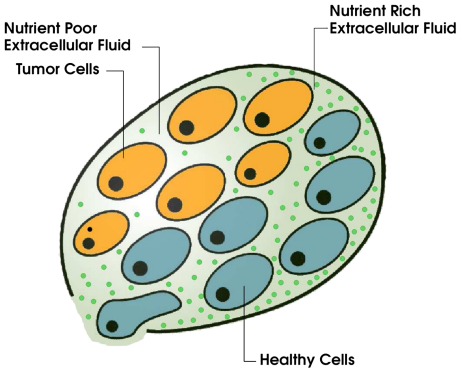

Figure 1. Four-species model: illustration of the four-species mixture. The tumor and healthy cell populations are assumed to have a thin diffuse interface, whereas the nutrient-rich and nutrient-poor extracellular water are segregated by a wide smooth interface.

DOI: 10.1002/cnm

where $f(u)$ is the classical Cahn–Hilliard free-energy density function, ϵ^2 is the diffusivity parameter for the surface energy term, $\chi(u,n)$ is the chemotaxis energy, and $\delta > 0$ is a small parameter governing the relative strength of the interaction among the cell and nutrient species.

As shown in [47], it is known that the forms of the equations for the balance of mass for each constituent are as follows:

$$\begin{aligned} u_t &= \nabla \cdot (M_u \nabla \mu_u) + \gamma_u, \\ h_t &= \nabla \cdot (M_h \nabla \mu_h) + \gamma_h, \\ n_t &= \nabla \cdot (M_n \nabla \mu_n) + \gamma_n, \\ w_t &= \nabla \cdot (M_w \nabla \mu_w) + \gamma_w. \end{aligned} \tag{5}$$

Note, that the densities ρ_i are assumed to be equal and constant, that is, $\rho_1 = \rho_2 = \cdots = C$, and that the velocities are taken to be negligible. The chemical potentials μ_i are determined through the form of the free energy by $\mu_i = D_{\phi_i} E$, where D_{ϕ_i} denotes the Gateaux derivative with respect to the variable ϕ_i. Constraints on the constitutive relations, as were derived in [47], provide guidance as to how to appropriately close this system of equations. In particular, the following relations must be satisfied:

$$\left.\begin{aligned} \gamma_u + \gamma_h + \nabla \cdot (M_u \nabla \mu_u) + \nabla \cdot (M_h \nabla \mu_h) = 0 \\ \gamma_n + \gamma_w + \nabla \cdot (M_u \nabla \mu_n) + \nabla \cdot (M_h \nabla \mu_w) = 0 \end{aligned}\right\}. \tag{6}$$

Additionally, it must hold that

$$\sum_i \mu_i \gamma_i \leqslant 0. \tag{7}$$

For the given form of the free energy, the forms of μ_i are as follows:

$$\left.\begin{aligned} \mu_u &= f'(u) - \epsilon^2 \Delta u + D_u \chi(u,n), \\ \mu_h &= -f'(C-h) + \epsilon^2 \Delta (C-h) - D_u \chi((C-h),n), \\ \mu_n &= D_n \chi(u,n) + \delta^{-1} n, \\ \mu_w &= -D_n \chi(u,(1-C)-w) - \delta^{-1}((1-C)-w), \end{aligned}\right\} \tag{8}$$

and it is easily verified that $\sum_i \mu_i = 0$. In particular, for $M_u = M_h$ and $M_n = M_w$, this means $\nabla(M_u \nabla \mu_u) + \nabla \cdot (M_h \nabla \mu_h) = 0$ and $\nabla \cdot (M_n \nabla \mu_n) + \nabla \cdot (M_w \nabla \mu_w) = 0$, which reduces the constraints in (6) to merely $\gamma_u + \gamma_h = 0$ and $\gamma_n + \gamma_w = 0$. One should note, if these constraints hold and $M_u = M_h$ and $M_n = M_w$, that Equations (5)a and (5)b are not independent nor are Equations (5)c and (5)d as $u_t + h_t = 0$ and $n_t + w_t = 0$. This is expected as $u_t + h_t = (u+h)_t = 1_t = 0$ and similarly for $n_t + w_t$, $n_t + w_t = (n+w)_t = 1_t = 0$. Thus, attention can be restricted to solving only two equations: the equations for u and for n. Explicitly written out, these are

$$\left.\begin{aligned} u_t &= \nabla \cdot \left(M_u \nabla \left(f'(u) - \epsilon^2 \Delta u + D_u \chi(u,n)\right)\right) + \gamma_u \\ n_t &= \nabla \cdot \left(M_n \nabla \left(D_n \chi(u,n) + \delta^{-1} n\right)\right) + \gamma_n \end{aligned}\right\} \tag{9}$$

with constraints (6) and (7).

Given these governing equations (9), one can show that the solution to these equations with $M_u = M_n = 1$ and with the given constraints satisfies the condition that the total energy is always non-increasing. Consider

$$\begin{aligned} \frac{\mathrm{d}}{\mathrm{d}t} E &= \int_\Omega \left(D_u E\, u_t + D_n E\, n_t\right) \mathrm{d}x = \int_\Omega \left(\mu_u u_t + \mu_n n_t\right) \mathrm{d}x \\ &= \int_\Omega \left(\mu_u \left(\Delta \mu_u + \gamma_u\right) + \mu_n \left(\Delta \mu_n + \gamma_n\right)\right) \mathrm{d}x \\ &= \int_\Omega \left(-\nabla \mu_u \cdot \nabla \mu_u - \nabla \mu_n \cdot \nabla \mu_n + \mu_u \gamma_u + \mu_n \gamma_n\right) \mathrm{d}x \\ &= -\|\nabla \mu_u\|_{L^2}^2 - \|\nabla \mu_n\|_{L^2}^2 + \int_\Omega \left(\mu_u \gamma_u + \mu_n \gamma_n\right) \mathrm{d}x. \end{aligned} \tag{10}$$

DOI: 10.1002/cnm

Thus, if γ_u and γ_n are chosen such that (7) holds, the energy is non-increasing. Note that this result would still hold for any semi-positive definite form for M_u and M_n. This is a natural result as the system is isothermal and thus having a thermodynamically consistent model is equivalent to having a system in which the energy is non-increasing; see for example [49].

3.1. Constitutive equations

It remains to specify specific forms for γ_u and γ_n as well as $\chi(u,n)$ and $f(u)$. For the mass exchange terms, it is anticipated that there will only be growth when there is some level of nutrient available. Further, the form should prevent growth if, because of numerical discretization, the solution takes on negative values.

Motivated by the linear phenomenological constitutive laws for chemical reactions (see, e.g., [50]) we propose the following:

$$\gamma_u = P(u)(\mu_n - \mu_u),$$
$$\gamma_n = -\gamma_u,$$

where $P(u)$ is a positive function defined as

$$P(u) = \begin{cases} \delta P_0 u & u \geqslant 0, \\ 0 & \text{elsewhere}, \end{cases}$$

with δ a small positive constant and $P_0 \geqslant 0$. Note that for this choice of γ_i, we indeed satisfy (7).

As δ is expected to be very small, one can notice that the most influential term within these mass exchange terms is $P_0 u n$. Indeed,

$$\gamma_u = P_0 u n + \delta P_0 u\big(D_n \chi(u,n) - \mu_u\big)$$

(provided $u \geqslant 0$). This implies that the effects of the additional terms should be minimal. Further investigation of their interpretation and influence is left as future work. Additionally, we comment that this particular form of $P(u)$ is the simplest form to help prevent compounding numerical instabilities in the case that the tumor concentration becomes negative because of numerical discretization. Modifications could also be made to further prevent tumor growth above the physically allowed value of 1, determined by the assumptions of mixture theory and the form of the free energy.

Regarding the terms in the free energy, the homogeneous free energy function $f(u)$ is chosen to be a double well with a quartic polynomial form,

$$f(u) = \Gamma u^2 (1-u)^2 . \tag{11}$$

This term provides the mechanism for phase separation favoring the states $u = 0$ and $u = 1$. The form of χ should be chosen such that for values of $u \in [0,1]$ and $n \in [0,1]$, the preferred energy state, that is, the lowest energy value, is when both $u = 1$ and $n = 1$. Although there are many forms that can satisfy these conditions, for simplicity, the form chosen here is the linear product

$$\chi(u,n) = -\chi_0 u n, \tag{12}$$

with χ_0 a positive constant. The sum of $f(u)$ and $\chi(u,n)$ can now be viewed as the homogeneous free energy. The plot of this summation on the domain $u \in [0,1]$ and $n \in [0,1]$ is shown in Figure 2. One can see that the lowest energy state is indeed where $u = 1$ and $n = 1$.

4. DISCRETIZATIONS

4.1. Weak form

Before writing out the weak form, we specify the boundary conditions to be of the homogeneous Neumann form. Additionally, for ease of implementation, it is chosen here to split the fourth-order

DOI: 10.1002/cnm

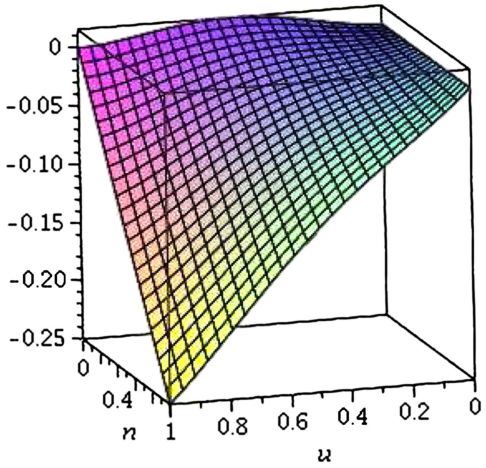

Figure 2. Graph of homogeneous free energy: $f(u) + \chi(u,n)$. ($\Gamma = \chi_0 = 0.25$).

differential equation into two second-order differential equations:

$$\begin{aligned}
u_t &= \nabla\left(M_u \nabla \mu_u\right) + \gamma_u && \text{for } (\mathbf{x},t) \in \Omega \times (0,T] \\
\mu_u &= f'(u) - \epsilon^2 \Delta u + D_u \chi(u,n) && \text{for } (\mathbf{x},t) \in \Omega \times (0,T] \\
n_t &= \nabla\left(M_n \nabla \mu_n\right) + \gamma_n && \text{for } (\mathbf{x},t) \in \Omega \times (0,T] \\
\mu_n &= D_n \chi(u,n) + \delta^{-1} n && \text{for } (\mathbf{x},t) \in \Omega \times (0,T] \\
\nabla u \cdot \mathbf{n} &= \nabla n \cdot \mathbf{n} = \nabla \mu_u \cdot \mathbf{n} = \nabla \mu_n \cdot \mathbf{n} = 0 && \text{for } (\mathbf{x},t) \in \partial\Omega \times (0,T] \\
u(\boldsymbol{x},0) &= u_0, \quad n(\boldsymbol{x},0) = n_0 && \text{for } \mathbf{x} \in \Omega.
\end{aligned} \tag{13}$$

Proceeding formally by multiplying by a test function and integrating by parts, the following weak form of (13) is obtained:

Find $(u, \mu_u, n, \mu_n) \in \mathcal{U}$ such that

$$\langle u_t, v\rangle + \langle n_t, z\rangle + B\left((u,\mu_u,n,\mu_n);(v,\mu_v,z,\mu_z)\right) = 0 \qquad \forall\ (v,\mu_v,z,\mu_z) \in \mathcal{V}, \tag{14}$$

where $\langle\cdot,\cdot\rangle$ is the appropriate duality pairing between u_t and v and for n_t and z and

$$\begin{aligned}
B\left((u,\mu_u,n,\mu_n);(v,\mu_v,z,\mu_z)\right) = &\int_\Omega (-\gamma_u)\, v \,\mathrm{d}x + \int_\Omega M_u \nabla \mu_u \nabla v \,\mathrm{d}x \\
&+ \int_\Omega \left(\mu_u - f'(u) - D_u \chi(u,n)\right) \mu_v \,\mathrm{d}x \\
&- \int_\Omega \epsilon^2 \nabla u \nabla \mu_v \,\mathrm{d}x + \int_\Omega (-\gamma_n)\, z \,\mathrm{d}x \\
&+ \int_\Omega M_n \nabla \mu_n \nabla z \,\mathrm{d}x + \int_\Omega \left(\mu_n - D_n \chi(u,n) - \delta^{-1} n\right) \mu_z \,\mathrm{d}x.
\end{aligned} \tag{15}$$

The well-posedness of the above weak formulation (15) is not considered here but will be studied elsewhere [51].

4.2. Discrete-time, continuous-space schemes

In this section, a semi-implicit time-discretization scheme is proposed on the basis of the concept that the free energy may be decomposed into the difference of two convex energies, that is,

$$E(u,n) = E_c(u,n) - E_e(u,n), \tag{16}$$

DOI: 10.1002/cnm

where both E_c and E_e are convex. That is, the energy can be seen as being composed of an expanding part and a contracting part. The fundamental idea is to treat the contracting, more stable, part implicitly and the expanding part explicitly. Schemes based on this fundamental idea form an attractive class of robust schemes for time integration for gradient flow systems, such as Cahn–Hilliard type problems. This general concept is not new, as it was discussed by Eyre in [52], and has been utilized in many other papers such as [53,54], but it must be reconsidered and reformulated for each new form of the energy functional. Although such a splitting always exists, it is by no means unique and the different forms may provide alternate benefits. For example, in this analysis, the splitting is performed in such a way that the resulting system of equations is linear. In particular, the functions are taken as follows:

$$\begin{aligned} E_c(u,n) &= \int_\Omega \left(f_c(u) + \frac{\epsilon^2}{2}|\nabla u|^2 + \chi_c(u,n) + \frac{n^2}{2\delta} \right) \mathrm{d}x \\ &= \int_\Omega \left(\frac{3\Gamma}{2}u^2 + \frac{\epsilon^2}{2}|\nabla u|^2 - \chi_0 u n + \frac{\alpha}{2}n^2 + \frac{n^2}{2\delta} \right) \mathrm{d}x \end{aligned} \tag{17}$$

$$\begin{aligned} -E_e(u,n) &= \int_\Omega \left(f_e(u) + \chi_e(u,n) \right) \mathrm{d}x \\ &= \int_\Omega \left(\Gamma\left(u^4 - 2u^3 + \frac{1}{2}u^2 \right) - \frac{\alpha}{2}n^2 \right) \mathrm{d}x, \end{aligned} \tag{18}$$

where α is a constant chosen larger than $\chi_0^2/(3\Gamma)$ to guarantee that for all χ_0 and Γ the convexity will not be violated. In the later numerical examples, $\alpha = \chi_0^2/(3\Gamma)+0.1$. These α terms cancel with each other in the sum $E_c - E_e$ and so are not actually being added to the free energy; rather, they provide a convenient way to ensure convexity. It should also be noted that the splitting of $f(u)$ will only maintain the proper convexity for values of u in approximately $[-0.55, 1.14]$. This is generally satisfied so long as χ_0 is not too much larger than Γ. A few examples are discussed later.

Lemma 4.1
Fundamental splitting inequality: Consider a domain Ω and suppose $(\phi,\psi),(\pi,\sigma) : \Omega^2 \to \mathbb{R}$ are such that $\nabla\phi\cdot\mathbf{n} = \nabla\psi\cdot\mathbf{n} = \nabla\pi\cdot\mathbf{n} = \nabla\sigma\cdot\mathbf{n} = 0$ on $\partial\Omega$. Consider the splitting of the energy E in (4) as $E = E_c - E_e$ as defined in (17) and (18) respectively. Then,

$$\begin{aligned} E(\phi,\psi) - E(\pi,\sigma) \leqslant &\left(D_\phi E_c(\phi,\psi) - D_\phi E_e(\pi,\sigma), \phi - \pi\right)_{L^2} \\ &+ \left(D_\psi E_c(\phi,\psi) - D_\psi E_e(\pi,\sigma), \psi - \sigma\right)_{L^2} \end{aligned} \tag{19}$$

where $D_\cdot$ denotes the variational derivative.

Proof
Let $E_c(\phi,\psi) = \int_\Omega e_c\left(\phi, \partial_x\phi, \partial_y\phi, \psi\right)\,\mathrm{d}x$. As $e_c(\boldsymbol{\alpha})$, where $\boldsymbol{\alpha} = \left(\phi, \partial_x\phi, \partial_y\phi, \psi\right)$, is convex in all of its arguments, the following statement holds:

$$e_c(\boldsymbol{\beta}) - e_c(\boldsymbol{\alpha}) \geqslant \nabla_{\boldsymbol{\alpha}} e_c(\boldsymbol{\alpha})\cdot(\boldsymbol{\beta}-\boldsymbol{\alpha}) \tag{20}$$

for any $\boldsymbol{\alpha}$ and $\boldsymbol{\beta} \in \mathbb{R}^4$. Setting $\boldsymbol{\alpha} = \left(\phi, \partial_x\phi, \partial_y\phi, \psi\right)$ and $\boldsymbol{\beta} = \left(\pi, \partial_x\pi, \partial_y\pi, \sigma\right)$ and integrating (20), it follows that

$$\begin{aligned} E_c(\pi,\sigma) - E_c(\phi,\psi) &= \int_\Omega e_c(\boldsymbol{\beta})\,\mathrm{d}x - \int_\Omega e_c(\boldsymbol{\alpha})\,\mathrm{d}x \\ &\geqslant \int_\Omega \nabla_{\boldsymbol{\alpha}} e_c(\boldsymbol{\alpha})\cdot(\boldsymbol{\beta}-\boldsymbol{\alpha})\,\mathrm{d}x \\ &= \int_\Omega \left\{ \partial_\phi e_c(\alpha)(\pi-\phi) + \partial_{\partial_x\phi} e_c(\alpha)(\partial_x\psi - \partial_x\phi) \right. \\ &\qquad \left. + \partial_{\partial_y\phi} e_c(\alpha)\left(\partial_y\psi - \partial_y\phi\right) + \partial_\psi e_c(\alpha)(\sigma-\psi) \right\} \mathrm{d}x. \end{aligned} \tag{21}$$

DOI: 10.1002/cnm

Integration by parts leads to inequality

$$\begin{aligned} E_c(\pi,\sigma) - E_c(\phi,\psi) \geqslant & \left(D_\phi E_c(\phi,\psi), \pi-\phi\right)_{L^2} \\ & + \left(D_\psi E_c(\phi,\psi), \sigma-\psi\right)_{L^2}. \end{aligned} \tag{22}$$

A similar analysis on E_e, but reversing the roles of $\boldsymbol{\alpha}$ and $\boldsymbol{\beta}$, results in

$$\begin{aligned} E_e(\phi,\psi) - E_e(\pi,\sigma) \geqslant & \left(D_\phi E_e(\pi,\sigma), \phi-\pi\right)_{L^2} \\ & + \left(D_\psi E_e(\pi,\sigma), \psi-\sigma\right)_{L^2}. \end{aligned} \tag{23}$$

Adding (22) and (23) yields

$$\begin{aligned} E(\pi,\sigma) - E(\phi,\psi) &= E_c(\pi,\sigma) - E_e(\pi,\sigma) - (E_c(\phi,\psi) - E_e(\phi,\psi)) \\ &\geqslant \left(D_\phi E_c(\phi,\psi), \pi-\phi\right)_{L^2} \\ &\quad + \left(D_\psi E_c(\phi,\psi), \sigma-\psi\right)_{L^2} \\ &\quad + \left(D_\phi E_e(\pi,\sigma), \phi-\pi\right)_{L^2} \\ &\quad + \left(D_\psi E_e(\pi,\sigma), \psi-\sigma\right)_{L^2} \\ &= \left(D_\phi E_c(\phi,\psi) - D_\phi E_e(\pi,\sigma), \pi-\phi\right)_{L^2} \\ &\quad + \left(D_\psi E_c(\phi,\psi) - D_\psi E_e(\pi,\sigma), \sigma-\psi\right)_{L^2}. \end{aligned} \tag{24}$$

□

In the spirit of the preceding lemma, the following semi-implicit scheme is proposed where s denotes the time step size:

$$\boxed{\begin{aligned} u^{k+1} - u^k &= s\nabla\cdot(M_u\nabla\tilde{\mu}_u) + \frac{s}{2}\left(P\left(u^{k+1}\right) + P\left(u^k\right)\right)(\tilde{\mu}_n - \tilde{\mu}_u), \\ n^{k+1} - n^k &= s\nabla\cdot(M_n\nabla\tilde{\mu}_n) - \frac{s}{2}\left(P\left(u^{k+1}\right) + P\left(u^k\right)\right)(\tilde{\mu}_n - \tilde{\mu}_u), \end{aligned}} \tag{25}$$

where $\tilde{\mu}_u$ and $\tilde{\mu}_n$ are defined as

$$\begin{aligned} \tilde{\mu}_u &= \mu_{u,c} - \mu_{u,e} = D_u E_c\left(u^{k+1}, n^{k+1}\right) - D_u E_e\left(u^k, n^k\right), \\ \tilde{\mu}_n &= \mu_{n,c} - \mu_{n,e} = D_n E_c\left(u^{k+1}, n^{k+1}\right) - D_n E_e\left(u^k, n^k\right). \end{aligned} \tag{26}$$

Written in weak form, this is equivalent to

$$\begin{aligned} \left(u^{k+1} - u^k, w\right) + s\left(M_u\nabla\tilde{\mu}_u, \nabla w\right) - s\left(\frac{1}{2}\left(P\left(u^{k+1}\right) + P\left(u^k\right)\right)(\tilde{\mu}_n - \tilde{\mu}_u), w\right) &= 0, \\ \left(\tilde{\mu}_u, \mu_w\right) - \left(D_u E_c\left(u^{k+1}, n^{k+1}\right) - D_u E_e\left(u^k, n^k\right), \mu_w\right) &= 0, \\ \left(n^{k+1} - n^k, z\right) + s\left(M_n\nabla\tilde{\mu}_n, \nabla z\right) + s\left(\frac{1}{2}\left(P\left(u^{k+1}\right) + P\left(u^k\right)\right)(\tilde{\mu}_n - \tilde{\mu}_u), z\right) &= 0, \\ \left(\tilde{\mu}_n, \mu_z\right) - \left(D_n E_c\left(u^{k+1}, n^{k+1}\right) - D_n E_e\left(u^k, n^k\right), \mu_z\right) &= 0. \end{aligned} \tag{27}$$

Theorem 4.2

Discrete gradient stability: If the mobility functions M_u and M_n are non-negative for all values of u and n, and the quantities u, n, μ_u, and μ_n are each continuous and differentiable, the time-stepping scheme as defined by (25) and (26) has the following properties:

1. The scheme is unconditionally gradient stable.
2. It is first order accurate.
3. It is mass conserving in the sense of $\int_\Omega \left(u^{k+1} + n^{k+1}\right)\,\mathrm{d}x = \int_\Omega \left(u^k + n^k\right)\,\mathrm{d}x$.

DOI: 10.1002/cnm

Proof

1. Using the fact that M_u, M_n and $P(u)$ are non-negative for all u and n, it follows from Lemma 4.1 that

$$\begin{aligned} E\left(u^{k+1},n^{k+1}\right)-E\left(u^{k},n^{k}\right) &\leqslant \left(D_u E_c\left(u^{k+1},n^{k+1}\right)-D_u E_e\left(u^{k},n^{k}\right),u^{k+1}-u^{k}\right)_{L^2} \\ &\quad+\left(D_n E_c\left(u^{k+1},n^{k+1}\right)-D_n E_e\left(u^{k},n^{k}\right),n^{k+1}-n^{k}\right)_{L^2} \\ &= s\left(\tilde{\mu}_u,\nabla\cdot\left(M_u\nabla\tilde{\mu}_u\right)+\frac{1}{2}\left(P\left(u^{k+1}\right)+P\left(u^{k}\right)\right)\left(\tilde{\mu}_n-\tilde{\mu}_u\right)\right) \\ &\quad+s\left(\tilde{\mu}_n,\nabla\cdot\left(M_n\nabla\tilde{\mu}_n\right)-\frac{1}{2}\left(P\left(u^{k+1}\right)+P\left(u^{k}\right)\right)\left(\tilde{\mu}_n-\tilde{\mu}_u\right)\right) \\ &= -s\left(\nabla\tilde{\mu}_u,M_u\nabla\tilde{\mu}_u\right)-s\left(\nabla\tilde{\mu}_n,M_n\nabla\tilde{\mu}_n\right) \\ &\quad-s\left(\frac{1}{2}\left(P\left(u^{k+1}\right)+P\left(u^{k}\right)\right)\left(\tilde{\mu}_n-\tilde{\mu}_u\right),\tilde{\mu}_n-\tilde{\mu}_u\right) \\ &\leqslant 0. \end{aligned} \tag{28}$$

Thus,

$$E\left(u^{k+1},n^{k+1}\right)\leqslant E\left(u^{k},n^{k}\right), \tag{29}$$

implying that the scheme is unconditionally energy gradient stable. That is, the energy will decrease at every time step independent of the step size.

2. Under sufficient smoothness, the following standard Taylor series expansions apply:

$$\begin{aligned} u\left(t_{k+1}\right) &= u\left(t_{k+1/2}\right)+\frac{s}{2}\frac{\mathrm{d}u\left(t_{k+1/2}\right)}{\mathrm{d}t}+O\left(s^2\right) \\ &= u\left(t_{k+1/2}\right) \\ &\quad+\frac{s}{2}\left(M_u\Delta\mu_u\left(t_{k+1/2}\right)+P\left(u\left(t_{k+1/2}\right)\right)\left(\mu_n\left(t_{k+1/2}\right)-\mu_u\left(t_{k+1/2}\right)\right)\right)+O\left(s^2\right) \end{aligned} \tag{30}$$

$$\begin{aligned} u\left(t_{k}\right) &= u\left(t_{k+1/2}\right)-\frac{s}{2}\frac{\mathrm{d}u\left(t_{k+1/2}\right)}{\mathrm{d}t}+O\left(s^2\right) \\ &= u\left(t_{k+1/2}\right) \\ &\quad-\frac{s}{2}\left(M_u\Delta\mu_u\left(t_{k+1/2}\right)+P\left(u\left(t_{k+1/2}\right)\right)\left(\mu_n\left(t_{k+1/2}\right)-\mu_u\left(t_{k+1/2}\right)\right)\right)+O\left(s^2\right). \end{aligned} \tag{31}$$

Taking the difference of these two equations gives

$$\begin{aligned} u\left(t_{k+1}\right)-u\left(t_{k}\right) =& s\left(M_u\Delta\mu_u\left(t_{k+1/2}\right)\right. \\ &\left.+P\left(u\left(t_{k+1/2}\right)\right)\left(\mu_n\left(t_{k+1/2}\right)-\mu_u\left(t_{k+1/2}\right)\right)\right)+O\left(s^2\right). \end{aligned} \tag{32}$$

Further,

$$\begin{aligned} \mu_{u,c}\left(t_{k+1}\right) &= \mu_{u,c}\left(t_{k+1/2}\right)+\frac{s}{2}\frac{\mathrm{d}\mu_{u,c}\left(t_{k+1/2}\right)}{\mathrm{d}t}+O\left(s^2\right), \\ \mu_{u,e}\left(t_{k}\right) &= \mu_{u,e}\left(t_{k+1/2}\right)-\frac{s}{2}\frac{\mathrm{d}\mu_{u,e}\left(t_{k+1/2}\right)}{\mathrm{d}t}+O\left(s^2\right). \end{aligned} \tag{33}$$

DOI: 10.1002/cnm

Taking the difference, these last two equations gives

$$\tilde{\mu}_u = \mu_{u,c}\left(t_{k+1}\right) - \mu_{u,e}\left(t_k\right) = \mu_u\left(t_{k+1/2}\right) + \frac{s}{2}\frac{\mathrm{d}\mu_u\left(t_{k+1/2}\right)}{\mathrm{d}t} + O\left(s^2\right). \tag{34}$$

A similar result holds for $\tilde{\mu}_n$. So, rearranging terms and inserting these estimates for $\mu_u\left(t_{k+1/2}\right)$ and $\mu_n\left(t_{k+1/2}\right)$ into (32),

$$u\left(t_{k+1}\right) - u\left(t_k\right) = s\left(M_u \Delta\tilde{\mu}_u + P\left(u\left(t_{k+1/2}\right)\right)\left(\tilde{\mu}_n - \tilde{\mu}_u\right)\right) + O\left(s^2\right). \tag{35}$$

Finally, it can be shown in a similar manner that

$$\frac{1}{2}\left(P\left(u\left(t_{k+1}\right)\right) + P\left(u\left(t_k\right)\right)\right) = P\left(u\left(t_{k+1/2}\right)\right) + O\left(s^2\right). \tag{36}$$

Inserting this into (35) completes the proof.

3. Adding (27)a and (27)c and testing against the test functions $w = 1$ and $z = 1$ gives

$$\int_\Omega \left(u^{k+1} + n^{k+1}\right) - \left(u^k + n^k\right)\,\mathrm{d}x = 0. \tag{37}$$

□

4.3. Fully discrete finite element approximations

The construction of fully discrete conforming finite element approximations of the system (15) is now discussed. Such a formulation involves a discretization of the spatial variations of (u, μ_u, n, μ_n) keeping, for the moment, the time variations continuous in time.

Let $\mathcal{T}^h$ denote a member of a family of partitions of domain Ω into meshes of non-overlapping convex finite elements Ω_k such that $\overline{\Omega} = \bigcup_{k=1}^{N(h)} \overline{\Omega}_k$ and $\Omega_k \cap \Omega_j = \emptyset,\ k \neq j$. Each Ω_k is the image of a master element $\tilde{\Omega}$ under an invertible (generally affine) map F_k. Define the finite-dimensional subspaces of $H^1(\Omega)$ and $H_0^1(\Omega)$ by

$$\mathcal{S}^h := \left\{v^h \in H^1(\Omega) : v^h|_{\Omega_k} = \hat{v} \circ F_k^{-1}, 1 \leqslant k \leqslant N(h), \hat{v} \in \mathbb{P}^K\left(\overline{\tilde{\Omega}}\right)\right\}, \tag{38}$$

and $\mathcal{S}_0^h := \mathcal{S}^h \cap H_0^1(\Omega)$, respectively. Here, $\mathbb{P}^K(\tilde{\Omega})$ is either the space of polynomials of degree $\leqslant K$ defined on the closure of $\tilde{\Omega}$ or the space of tensor products of polynomials of degree K on the closure of $\tilde{\Omega}$. With these notations and conventions in place, the semi-discrete approximation $\mathbf{u}^h := (u^h, \mu_u^h, n^h, \mu_n^h) : [0, T] \to \mathcal{S}^h \times \mathcal{S}^h \times \mathcal{S}^h \times \mathcal{S}^h$ is defined as follows:

$$\left(u_t^h(t), \varphi^h\right) + \left(n_t^h(t), \zeta^h\right) + B(\mathbf{u}^h(t); \mathbf{w}^h) = 0 \quad \forall \mathbf{w}^h := (\varphi^h, \eta^h, \zeta^h, \xi^h) \in \mathcal{S}^h \times \mathcal{S}^h \times \mathcal{S}^h \times \mathcal{S}^h, \tag{39}$$

for a.e. $t \in (0, T)$. The initial conditions for u^h and n^h are set by $u^h(0) = \mathcal{I}^h u_0$, and $n^h(0) = \mathcal{I}^h n_0$ where $\mathcal{I}^h : H^1(\Omega) \to \mathcal{S}^h$ is a suitable interpolation or projection.

Denote by $\{\varphi_i(\mathbf{x})\}_{i=1}^N$ a set of basis functions of $\mathcal{S}^h$ generated on a partition $\mathcal{T}^h$ by the finite element approximations: $\mathcal{S}^h = \operatorname{span}\{\varphi_i\}$. Then, each of the component approximations is of the form

$$\begin{aligned} u^h(t, \mathbf{x}) &= \sum_{i=1}^N u_i(t)\,\varphi_i(\mathbf{x}), \quad \mu_u^h(t, \mathbf{x}) = \sum_{i=1}^N \mu_{u,i}(t)\,\varphi_i(\mathbf{x}), \\ n^h(t, \mathbf{x}) &= \sum_{i=1}^N n_i(t)\,\varphi_i(\mathbf{x}), \quad \mu_n^h(t, \mathbf{x}) = \sum_{i=1}^N \mu_{n,i}(t)\,\varphi_i(\mathbf{x}). \end{aligned} \tag{40}$$

Here, $u_i(t)$, $\mu_{u,i}(t)$, $n_i(t)$, and $\mu_{n,i}(t)$ are continuous functions in time. Upon introducing these into (39), we obtain a system of nonlinear ODE in the unknown discrete variables, $u_i(t)$, $\mu_{u,i}(t)$, $n_i(t)$, and $\mu_{n,i}(t)$. The fully discrete system is thus created by the combination of the semi-implicit time-stepping algorithm (25) with the mixed finite element approximation (39).

DOI: 10.1002/cnm

5. NUMERICAL EXAMPLES

We begin with an example to illustrate the mass conservation property of the time-stepping algorithm. For this example, we consider $\hat{D} = 1$, $\hat{M} = 200$, $P_0 = 0.1$, $\chi_0 = 0.05$, $\delta = 0.01$, $\epsilon = 0.005$, and $\Gamma = 0.045$. The initial condition for the tumor is set as a small ellipse, and the nutrient is set to the value 1, where $\Omega = [-1, 1]^2$. In Figure 3, the initial conditions of the tumor and the nutrient are shown on the left and in the right the concentrations at a later time. Figure 4 shows the graph of the total mass in the system over time, $\int_\Omega n + c \, dx$, and the energy in the system. Together, Figures 3 and 4 illustrate the dynamics of the nutrient in the system converting into tumor in such a way as to

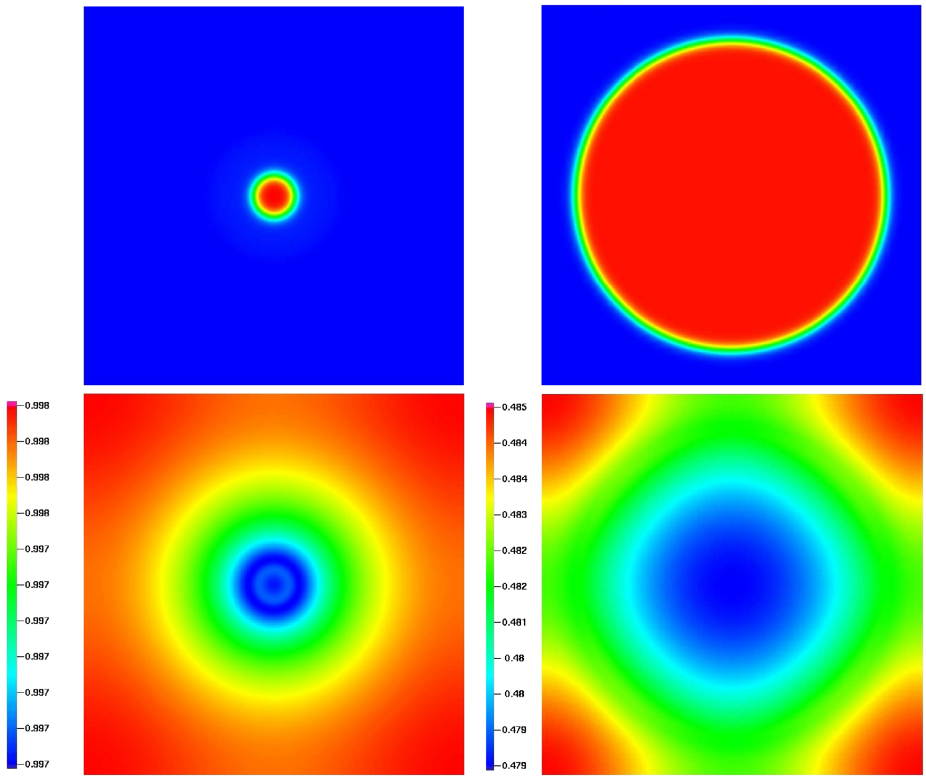

Figure 3. Snapshots of simulation with pure Neumann boundary conditions and non-steady state nutrient equation. Top row: tumor concentration at an earlier time (left) and a later time (right). Bottom row: nutrient concentration at same time points. Note that the scale on the nutrient is drastically different at these two points.

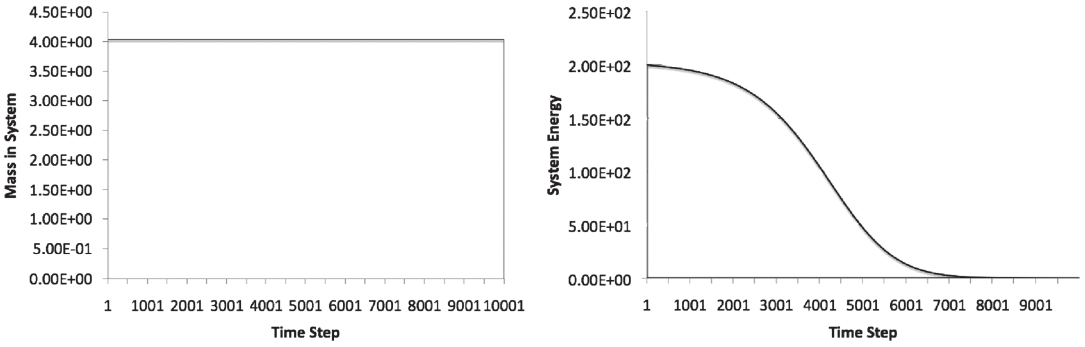

Figure 4. Right: plot of mass in system, $\int_\Omega u + n \, dx$, at each time step. Left: plot of total energy in system as given by (4). It is easily seen that the mass remains constant and the system energy is non-increasing.

DOI: 10.1002/cnm

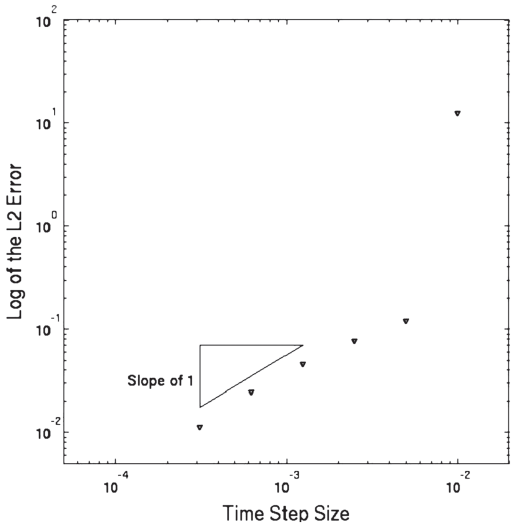

Figure 5. L^2 error in solution at $t = 1$: plot of L^2 error against a reference solution obtained with $s = 0.000078125$. A line with the expected slope of 1 is shown above the points.

conserve the total mass and that the energy of the system is non-increasing throughout this process. Experimentally computed convergence rates are depicted in Figure 5.

In the preceding example and sections, an analysis is described for a parabolic system of equations involving two unknowns with homogeneous Neumann boundary conditions. However, in the spirit of tumor growth modeling, for the numerical examples, two small modifications are made to this system regarding the nutrient-rich extracellular water. Namely, the nutrient concentration will be taken as quasi-steady, that is, $n_t = 0$ and Dirichlet boundary conditions will be imposed. These are reflective of the facts that the diffusion of nutrient within the domain happens on a much faster time scale than that of the tumor growth and movement and that the nutrient concentration will be at normal levels far from the tumor because of a continuous external supply. One should note that the assumed quasi-steady behavior of the nutrient-rich extracellular water corresponds to the limiting behavior of the fully unsteady system. Additionally, the mobilities are taken as follows: $M_u = \hat{M}u^2$ and $M_n = \delta\hat{D}$, where $\hat{M}$ and $\hat{D}$ are positive constants. The strong form of the system is thus written as follows.

Find u and n such that

$$\begin{aligned}
u_t &= \nabla\cdot\left(\hat{M}u^2\nabla\left(f'(u)-\epsilon^2\Delta u-\chi_0 n\right)\right)+\gamma_u && \text{for } (\mathbf{x},t)\in\Omega\times(0,T]\\
0 &= \nabla\cdot\left(\delta\hat{D}\nabla\left(\delta^{-1}n-\chi_0 u\right)\right)+\gamma_n && \text{for } (\mathbf{x},t)\in\Omega\times(0,T]\\
\nabla u\cdot\mathbf{n} &= 0, \quad n=1 && \text{for } (\mathbf{x},t)\in\partial\Omega\times(0,T]\\
u(\boldsymbol{x},0) &= u_0 && \text{for } \mathbf{x}\in\Omega.
\end{aligned} \tag{41}$$

Because of the added Dirichlet source of nutrients, one can no longer expect dissipation of the free energy as it is no longer an isolated system. However, it is not unreasonable to expect that a gradient-stable scheme, developed for an isolated system, will perform well in the Dirichlet case as well. Naturally, the Dirichlet boundary conditions are also expected to alter the mass conservation property.

As a first example, a two-dimensional simulation is considered on the domain $\Omega = [0, 25.6]^2$ with a tumor growing in a moderately oxygenated region, $\hat{D} = 1$, with a low proliferation rate $P_0 = 0.1$. As the initial condition, the tumor is taken to occupy the ellipsoidal domain

$$\left\{(x,y) : (x-12.8)^2/2.1 + (y-12.8)^2/1.9 \leqslant 1\right\}.$$

DOI: 10.1002/cnm

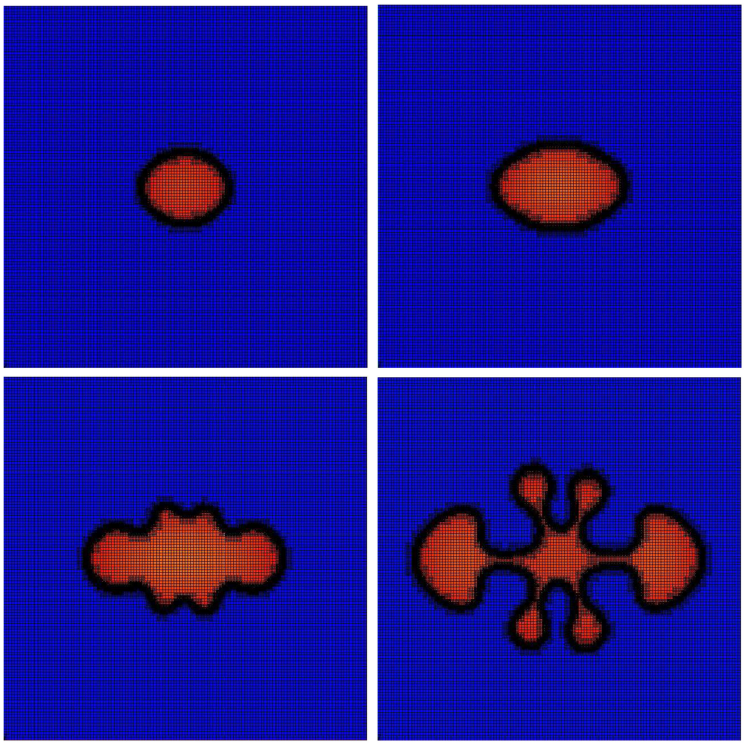

Figure 6. Adaptive meshing: illustration of the mesh adaptivity for the simulation shown in Figure 7. The patch-recovery method is used for the adaptive algorithm [55, 56].

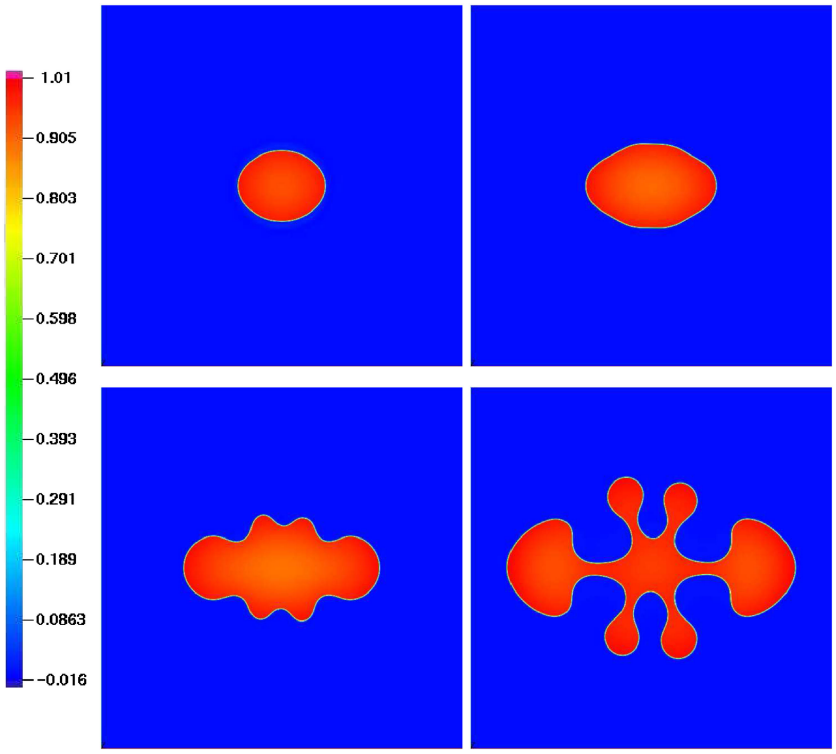

Figure 7. Example simulation: snapshots are shown at $t = 20, 40, 60$, and 80 of a simulation with $\Gamma = 0.045$, $\epsilon = 0.005$, $\chi_0 = 0.05$, $\delta = 0.01$, $P_0 = 0.1$, $\hat{M} = 200$, and $\hat{D} = 1$.

DOI: 10.1002/cnm

Key to all examples are the parameters used in the free energy; these are taken to be as follows: $\delta = 0.01$, $\Gamma = 0.045$, $\epsilon = 0.005$, and $\chi_0 = 0.05$. Rectangular mesh with C^0 bilinear shape functions are used.

Because of the need to resolve the interface while retaining the ability to perform computations in a timely manner, the patch-recovery algorithm is used for adaptive mesh refinement [55, 56]. This method utilizes patches of elements to estimate, via a L^2 projection, the value of the derivative of the solution at the nodal points $\boldsymbol{\sigma}^*$. This patch-recovery provides a more accurate approximation to the derivative at the nodes than the finite element solution's derivative $\boldsymbol{\sigma}$. Thus, it can be used in calculating the error indicators $\mathbf{e} = \boldsymbol{\sigma}^* - \boldsymbol{\sigma}$ to be used in mesh refinement. It is seen that this algorithm performs well at adapting appropriately around the interface as seen in Figure 6. The coarsest level of resolution on the mesh has $h = 25.6/64$ and the finest level has $h = 25.6/2048$. It should also be noted that there is at most one hanging node per element side.

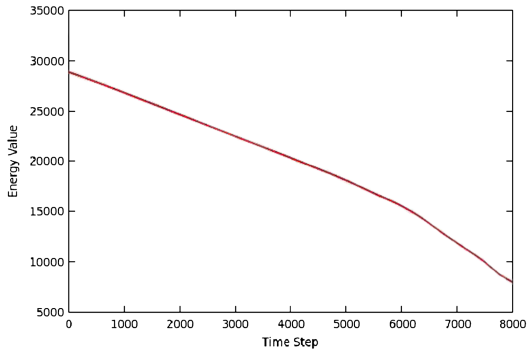

Figure 8. Simulation energy profile: shown here is the evolution of the energy value for the simulation shown in Figure 7 corresponding to (4) as a function of time step.

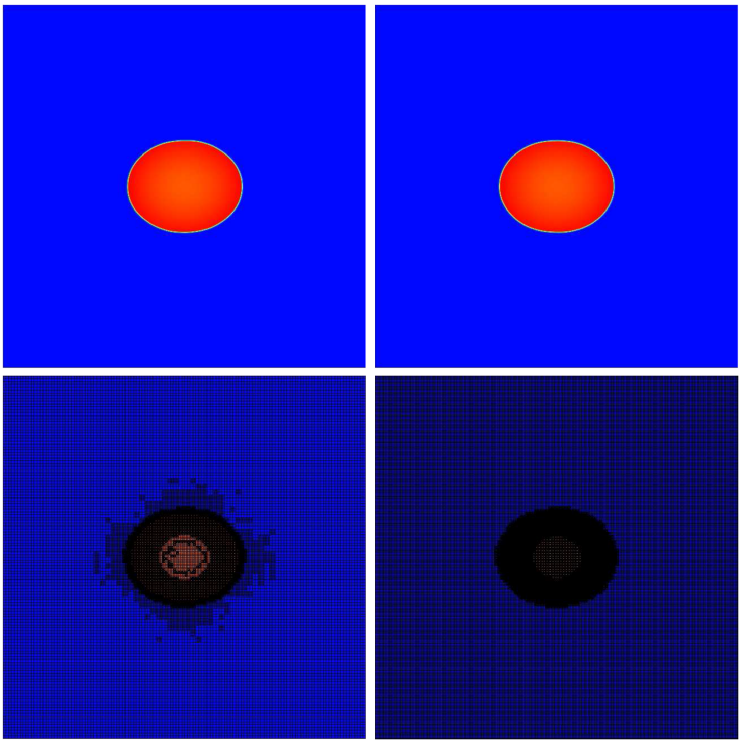

Figure 9. Evidence for spatial accuracy: on the top row, the solution at $t = 20$ is shown for the same set of parameters and initial conditions as in Figure 7, but with one mesh at a finer resolution than the other. The corresponding final meshes are shown below the solutions.

DOI: 10.1002/cnm

Figure 7 shows the evolution of the tumor concentration at times $t = 20$, 40, 60, and 80 having been calculated with a time step size $s = 0.01$. The tumor starts growing increasingly more ellipsoidal at first and eventually begins forming buds growing toward the higher levels of nutrient. The energy value (4) as a function of time step is also shown in Figure 8.

Also considered in this section is the order of accuracy of the time-stepping algorithm. The simulation was run for many different time step values, $s = 0.01$, 0.005, 0.0025, 0.00125, 0.000625, and 0.0003125. The solution at $t = 1$ was then compared with a reference solution computed with $s = 0.000078125$ to compute the L^2 error. As the scheme was shown to have a local truncation error of $O\left(s^2\right)$, the global error is expected to be proportional to the time step size s. The indicated convergence order of the points shown is about 1, as expected (see Figure 5). Spatial accuracy is also considered by solving the same problem with $s = 0.01$, but on a finer mesh. While the mesh adaptivity is still used, the coarsest level on the finer mesh is $h = 128/25.6$. The solution at $t = 20$ is shown in Figure 9 along with the final mesh. Although the qualitative similarity between these two solutions is not a proof of accuracy, they do provide support for the hypothesis.

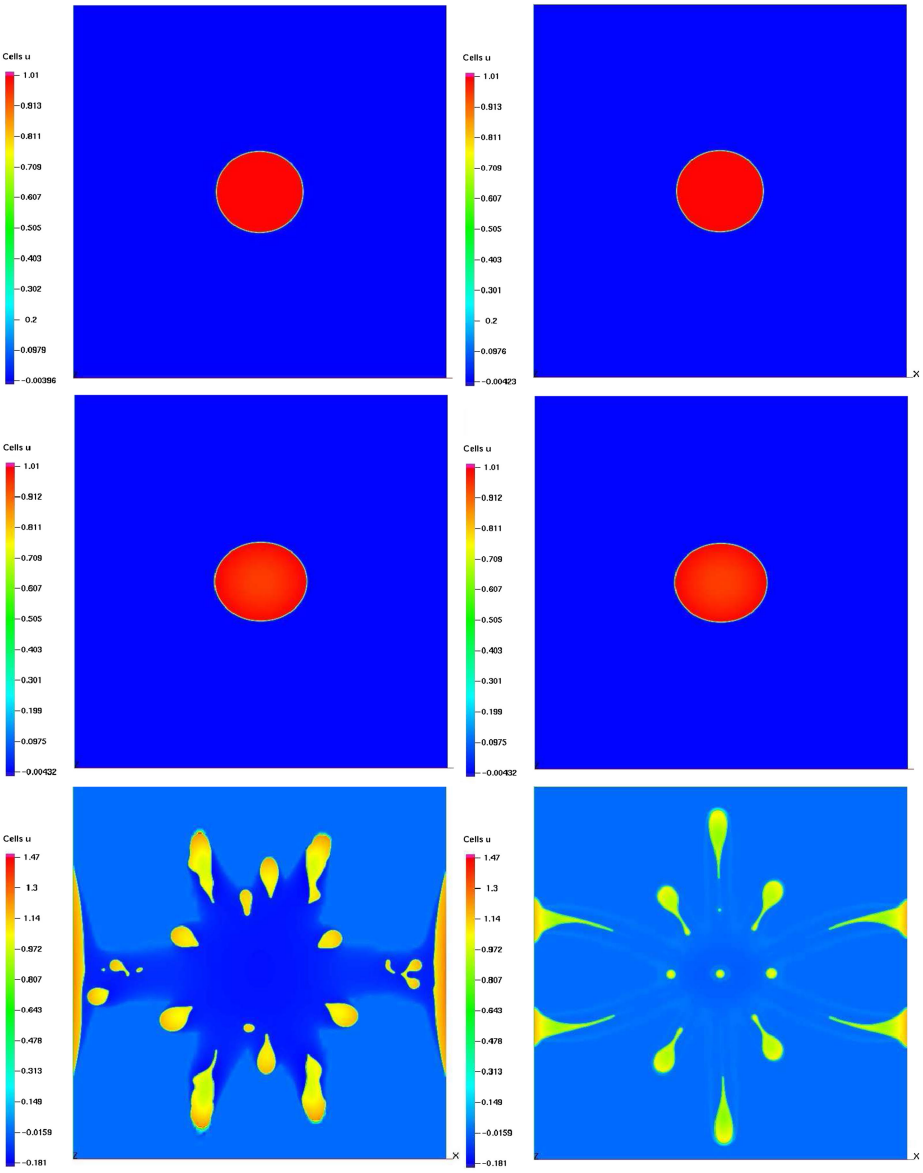

Figure 10. Effects of parameter χ_0: illustrated here are the effects of different values of χ_0 when $\Gamma = 0.045$ and $\epsilon = 0.005$ are held constant. In the first row, $\chi_0 = 0.005$; in the second row, $\chi_0 = 0.05$; and in the third row, $\chi_0 = 0.5$. In the first column, $\delta = 0.1$; and in the second column, $\delta = 0.01$.

DOI: 10.1002/cnm

5.1. *Parameter study*

As can be seen in the derivation of this model, it is ultimately the form of the free energy that drives the dynamics of the model. When looking at the chosen form, one can deduce that there are three terms of interest all in competition: the quartic, double-well term rendering the solution to prefer values of $u = 0$ and $u = 1$; the surface tension term involving gradients of u penalizing the length of the interface; and the chemotaxis term involving the interaction between the two species u and n, which drives the tumor concentration toward the regions of higher nutrient levels. Throughout this section, the time step used is $s = 0.01$ and the tumor is taken to occupy the ellipsoidal domain $\left\{(x, y) : (x - 12.8)^2 / 2.1 + (y - 12.8) / 1.9 \leqslant 1\right\}$ as the initial condition.

Figure 10 demonstrates the effect of holding $\epsilon = 0.005$ and $\Gamma = 0.045$ constant and letting χ_0 vary over different values, specifically $\chi_0 = 0.005, 0.05, 0.5$. As the parameter δ is varying the degree of dependence

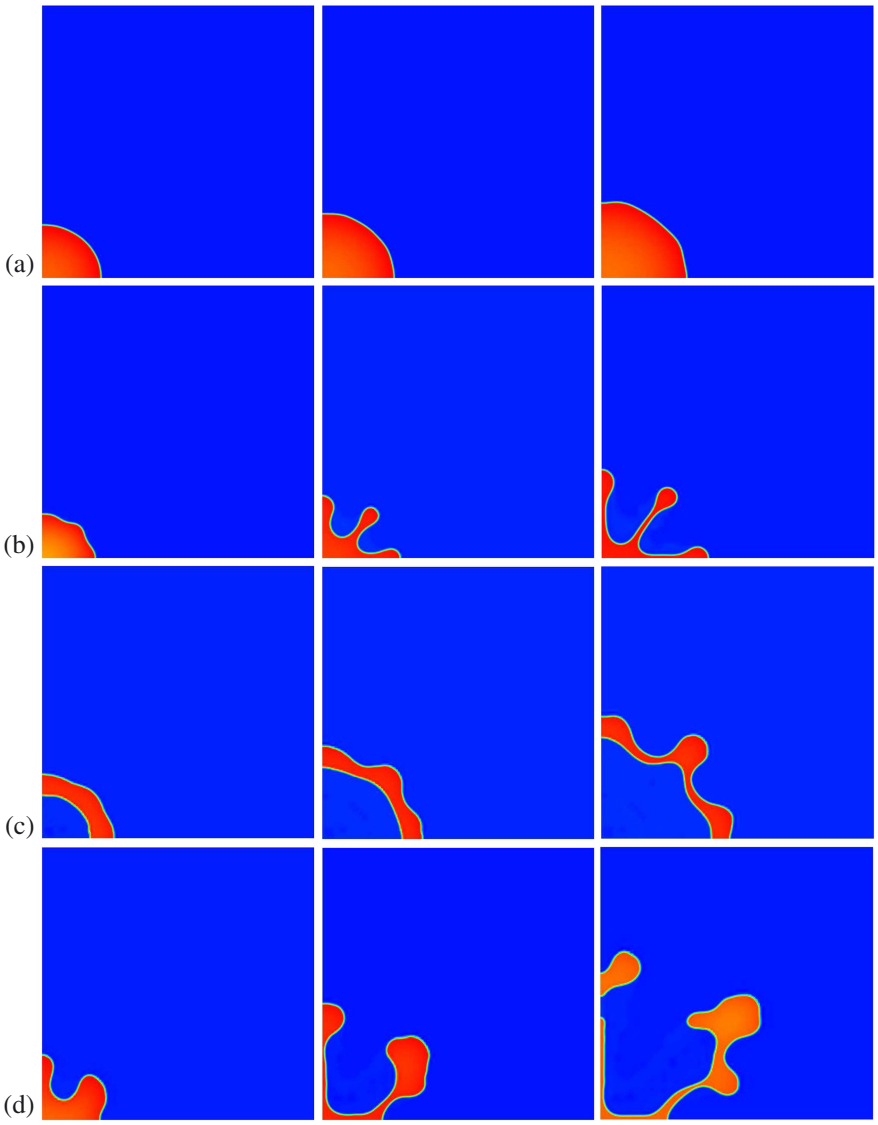

Figure 11. Effects of parameter combinations: in all simulations $\epsilon = 0.005$ and $\Gamma = 0.045$. Snapshots in the first column are at $t = 3$, in the second are at $t = 6$, and in the third are at $t = 9$. (a) $\hat{M} = 50$, $\hat{D} = 1.1$, $P_0 = 0.85$, $\chi_0 = 0.067$. (b) $\hat{M} = 86.6$, $\hat{D} = 0.2$, $P_0 = 0.5$, $\chi_0 = 0.067$. (c) $\hat{M} = 175$, $\hat{D} = 1.1$, $P_0 = 0.14$, $\chi_0 = 0.135$. (d) $\hat{M} = 290$, $\hat{D} = 1.1$, $P_0 = 0.5$, $\chi_0 = 0.067$.

DOI: 10.1002/cnm

the nutrient species has on the parameter χ_0, we also show the simulation outcomes for $\delta = 0.1$ and 0.01. The images seen in Figure 10 are all at $t = 12$.

One can see that when the ratio of χ_0 to Γ is small, the tumor remains circular and values of u remain very close to 0 and 1. However, when χ_0 and Γ are of approximately equal magnitude, while the tumor still takes on values of about 0 and 1, it is now starting to go into a stronger ellipse. Finally, when χ_0 is much larger than Γ and ϵ, one can see that u no longer takes on values close to 0 and 1. Rather, the tumor immediately breaks apart and begins moving quickly toward the regions with higher nutrients. Further, it is only when χ_0 has this very strong affect that the value of δ seems to make a difference in the simulation outcome.

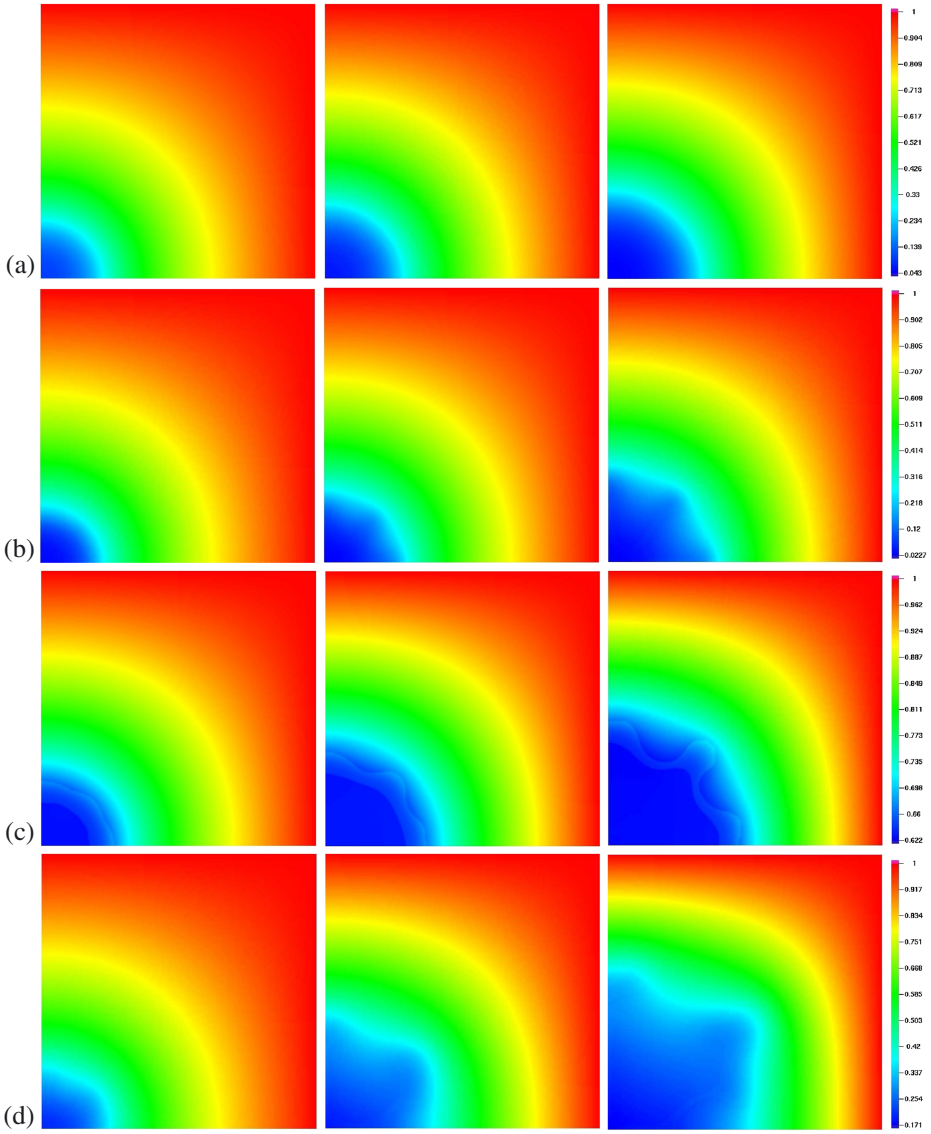

Figure 12. Effects of parameter combinations on nutrient: snapshots of nutrient profiles corresponding to tumor profiles in Figure 11. Snapshots in the first column are at $t = 3$, in the second are at $t = 6$, and in the third are at $t = 9$. (a) $\hat{M} = 50$, $\hat{D} = 1.1$, $P_0 = 0.85$, $\chi_0 = 0.067$. (b) $\hat{M} = 86.6$, $\hat{D} = 0.2$, $P_0 = 0.5$, $\chi_0 = 0.067$. (c) $\hat{M} = 175$, $\hat{D} = 1.1$, $P_0 = 0.14$, $\chi_0 = 0.135$. (d) $\hat{M} = 290$, $\hat{D} = 1.1$, $P_0 = 0.5$, $\chi_0 = 0.067$.

DOI: 10.1002/cnm

Also studied here are the effects of different values of P_0, $\hat{M}$, $\hat{D}$, and χ_0. Figure 5, 11 and 12 illustrates different behaviors seen for the tumor and nutrient concentrations, respectively. In this figure, the rows correspond to different parameter values and the columns correspond to snapshots at $t = 3$, $t = 6$, and $t = 9$. In the first row, the proliferation parameter and the nutrient diffusion parameter are relatively large; this combination, along with a low mobility, acts as a stabilizing force keeping the tumor compact. In the second row, the nutrient diffusion coefficient is small, resulting in lower levels of nutrient within the tumor region. This causes the tumor to form narrow protrusions moving toward the higher levels of oxygen. In the third row, the dominating parameter is χ_0. Thus, even though there is a relatively large amount of oxygen within the tumor ($\hat{D} = 1.1$), all the tumor cells move quickly toward the regions with higher nutrient levels. In the fourth row, despite the fact $\hat{D} = 1.1$ and thus there is a relatively high concentration of nutrient in the tumor, the mobility is also large, effectively allowing the tumor cells to move more quickly toward to nutrient. The evolution of the energy value is also shown for each of these simulations in Figure 13. It is observed that in

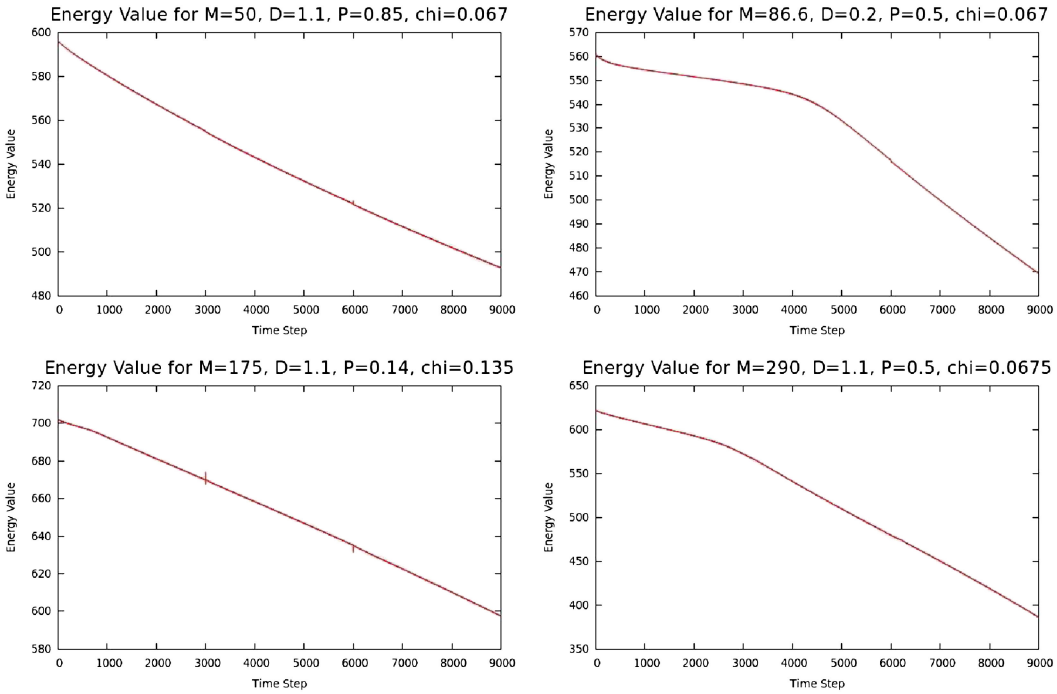

Figure 13. Energy profiles for parameter study: each plot shows the evolution of the energy value as a function of time step for the different simulations shown in Figure 11. The energy appears to always be non-increasing except for a few locations where simulation restarts occurred, causing a numerical artifact.

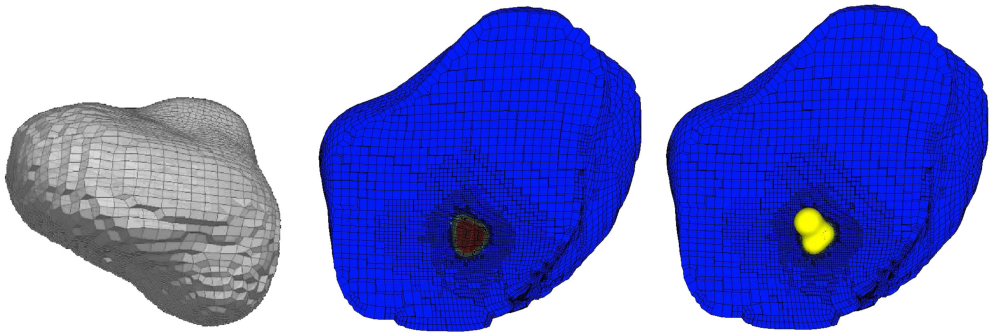

Figure 14. Three-dimensional simulation. Left: three-dimensional computational domain. A cutplane of the three-dimensional mesh intersecting the tumor is shown in the center at $t = 1.6$, and the same cutplane with the $u = 0.5$ isosurface plotted on top of it is shown on the right.

DOI: 10.1002/cnm

each simulation, the energy is non-increasing except for a few locations where the simulation was restarted. Thus, these apparent blips can be attributed to numerical artifacts.

Cristini *et al.* performed a linear stability analysis on a similar set of equations in [46] predicting similar results. Although these equations did not interpret the nutrient as a component of the mixture within the framework of mixture theory, it is expected that the same type of analysis on this current set of equations would result in very similar conclusions. The results seen in Figure 11 support this hypothesis.

5.2. Three-dimensional example

The choice to use the finite element method was made so that computations could be performed on more realistic biological domains, such as the prostate. Although this capability is not utilized throughout the rest of this document, the fact is illustrated in this section. As the three-dimensional case is even more computationally demanding, the same adaptivity regime is used as in the two-dimensional examples. A computational domain resembling a prostate is considered and is shown on the left in Figure 14. A tumor is seeded, not quite centered, within the prostate and is allowed to grow under moderate oxygenation conditions. The time step size is taken as $s = 0.01$. The parameters are taken as follows: $\hat{M} = 10$, $P_0 = 0.1$, $\hat{D} = 1$, $\chi_0 = 0.4$, $\delta = 0.01$, $\epsilon = 0.01$, and $\Gamma = 0.25$. The center and right images in Figure 14 shows a cutplane of the three-dimensional domain with an illustration of the mesh at $t = 1.6$.

6. CONCLUSIONS

In this paper, a four-species model is developed consisting of a tumor cell species, a healthy cell species, and two extracellular water species, one nutrient rich and one nutrient poor. This is the first tumor growth model based on the continuum theory of mixtures to include the oxygen species within the mixture and to present simulations for non-regular three-dimensional geometries. The model is shown to be thermodynamically consistent, and a time-stepping algorithm is paired with a mixed finite element spatial discretization to provide numerical examples illustrating the range of solutions that these equations can produce for various parameter values. A three-dimensional example is shown to demonstrate the capability of the finite element discretization for performing on general three-dimensional meshes.

ACKNOWLEDGEMENTS

The authors gratefully recognize the support by the Department of Energy under Award Number DE-FC52-08NA28615. Kris van der Zee acknowledges the support of the Nederlandse organisatie voor Wetenschappelijk Onderzoek (NWO) via the Innovational Research Incentives Scheme (IRIS), Veni grant 639.031.033.

REFERENCES

1. Bartlett JM, Stirling D. A Short History of the Polymerase Chain Reaction. In *Methods in Molecular Biology*, Vol. 226. Springer Protocols Humana Press, Totowa, August 2003.
2. Hanahan D, Weinburg RA. The hallmarks of cancer. *Cell* January 2000; **100**:57–70.
3. Araujo RP, McElwain DLS. A history of the study of solid tumour growth: the contribution of mathematical modelling. *Bulletin of Mathematical Biology* 2004; **66**:1039–1091.
4. Wodarz D, Komarova NL. *Computational Biology of Cancer: Lecture Notes and Mathematical Modeling*. World Scientific: Hackensak, NJ, 2005.
5. Bellomo N, Chaplain M, Angelis ED (eds). *Selected Topics in Cancer Modeling: Genesis, Evolution, Immune Competition, and Therapy*. Springer: London, 2008.
6. Bellomo N, Li NK, Maini PK. On the foundations of cancer modelling: selected topics, speculations, and perspectives. *Mathematical Models and Methods in Applied Sciences* 2008; **18**(4):593–646.
7. Preziosi L (ed.). *Cancer Modelling and Simulation*. Chapman & Hall/CRC: Boca Raton, 2003.
8. Lowengrub JS, Frieboes HB, Jin F, Chuang Y-L, Li X, Macklin P, Wise SM, Cristini V. Nonlinear modelling of cancer: bridging the gap between cells and tumours. *Nonlinearity* 2010; **23**(1):R1.
9. Byrne HM, Alarcón T, Owen MR, Webb SD, Maini PK. Modelling aspects of cancer dynamics: a review. *Philosophical Transactions of the Royal Society A* 2006; **364**:1563–1578.
10. Fasano A, Bertuzzi A, Gandolfi A. Mathematical modelling of tumour growth and treatment. In *Complex Systems in Biomedicine*, Quarteroni A, Formaggia L, Veneziani A (eds). Springer Milan: Milano, 2006; 71–108.
11. Graziano L, Preziosi L. Mechanics in tumor growth. In *Modelling of Biological Materials,* Chapter 7, Mollica F, Preziosi L, Rajagopal KR (eds). Birkhãser: Boston, 2007; 263–321.

DOI: 10.1002/cnm

12. Drasdo D, Hoehme S, Block M. On the role of physics in the growth and pattern formation of multi-cellular systems: what can we learn from individual-cell based models? *Journal of Statistical Physics* 2007; **128**:287–354.
13. Sanga S, Frieboes HB, Zheng X, Gatenby R, Bearer EL, Cristini V. Predictive oncology: a review of multidisciplinary, multiscale in silico modeling linking phenotype, morphology and growth. *NeuroImage* 2007; **37**(Supplement 1):S120–S134. Proceedings of the International Brain Mapping & Intraoperative Surgical Planning Society Annual Meeting, 2006.
14. Anderson ARA, Quaranta V. Integrative mathematical oncology. *Nature Reviews Cancer* 2008; **8**(3):227–234.
15. Roose T, Chapman SJ, Maini PK. Mathematical models of avascular tumor growth. *SIAM Review* 2007; **49**(2):179–208.
16. Hatzikirou H, Deutsch A, Schaller C, Simon M, Swanson K. Mathematical modeling of glioblastoma tumour development: a review. *Mathematical Models and Methods in Applied Sciences* 2005; **15**(11):1779–1794.
17. Harpold HLP, Alvord EC, Swanson KR. The evolution of mathematical modeling of glioma proliferation and invasion. *Journal of Neuropathology & Experimental Neurology* 2007; **66**(1):1–9.
18. Deisboeck TS, Zhang L, Yoon J. In silico cancer modeling: is it ready for prime time? *Nature Reviews Clinical Oncology* 2009; **6**:34–42.
19. van Leeuwen IMM, Edwards CM, Ilyas M, Byrne HM. Towards a multiscale model of colorectal cancer. *World Journal of Gastroenterology* 2007; **13**(9):1399–1407.
20. Friedman A. Mathematical analysis and challenges arising from models of tumor growth. *Mathematical Models and Methods in Applied Sciences* 2007; **17**:1751–1772.
21. Preziosi L, Tosin A. Multiphase and multiscale trends in cancer modelling. *Mathematical Modelling of Natural Phenomena* 2009; **4**(3):1–11.
22. Truesdell C, Toupin R. The classical field theories. In *Handbuch der Physik*, Vol. III/I, Flugge S (ed.). Springer-Verlag: Berlin, 1960.
23. Bowen RM. Theory of mixtures. In *Continuum Physics*, Vol. 3, Eringen AC (ed.). Academic Press: New York, 1976.
24. Please CP, Pettet GJ, McElwain DLS. A new approach to modelling the formation of necrotic regions in tumours. *Applied Mathematics Letters* 1998; **11**:89–94.
25. Please CP, Pettet GJ, McElwain DLS. Avascular tumour dynamics and necrosis. *Mathematical Models and Methods in Applied Sciences* 1999; **9**:569–579.
26. Breward CJW, Byrne HM, Lewis CE. The role of cell–cell interactions in a two phase model for avascular tumour growth. *Journal of Mathematical Biology* 2002; **45**:125–152.
27. Preziosi L, Farina A. On Darcy's law for growing porous media. *International Journal of Non-Linear Mechanics* 2001; **37**:485–491.
28. Araujo RP, McElwain DLS. A mixture theory for the genesis of residual stresses in growing tissues II: solutions to the biphasic equations for a multicell spheroid. *SIAM Journal on Applied Mathematics* 2005; **66**:447–467.
29. Ambrosi D, Preziosi L. Cell adhesion mechanisms and stress relaxation in the mechanics of tumours. *Biomechanics and modeling in mechanobiology* 2009; **8**(5):397–413.
30. Chaplain MAJ, Graziano L, Preziosi L. Mathematical modelling of the loss of tissue compression responsiveness and its role in solid tumour development. *Mathematical Medicine and Biology* 2006; **23**(3):197.
31. Preziosi L, Tosin A. Multiphase modelling of tumour growth and extracellular matrix interaction: mathematical tools and applications. *Journal of mathematical biology* 2009; **58**(4):625–656.
32. Tosin A, Preziosi L. Multiphase modeling of tumor growth with matrix remodeling and fibrosis. *Mathematical and Computer Modelling* 2010; **52**:969–976.
33. Breward CJW, Byrne HM, Lewis CE, A multiphase model describing vascular tumour growth. *Bulletin of Mathematical Biology* 2003; **65**:609–640.
34. Araujo RP, McElwain DLS. A linear-elastic model of anisotropic tumour growth. *European Journal of Applied Mathematics* 2004; **15**:365–384.
35. Chen YC, Byrne HM, King JR. The influence of growth-induced stress from the surrounding medium on the development of multicell spheroids. *Journal of Mathematical Biology* 2001; **43**:191–220.
36. Rodriguez EK, Hoger A, McCulloch AD. Stress-dependent finite growth in soft elastic tissues. *Journal of Biomechanics* 1994; **27**:455–467.
37. Skalak R, Zargaryan S, Jain RK, Netti PA, Hoger A. Compatibility and the genesis of residual stress by volumetric growth. *Journal of Mathematical Biology* 1996; **34**:889–914.
38. Boucher Y, Jain RK. Microvascular pressure is the principal driving force for interstitial hypertension in solid tumors: implications for vascular collapse. *Cancer Research* 1992; **51**:4264–4266.
39. Helmlinger G, Netti PA, Lichtenbeld HD, Melder RJ, Jain R K. Solid stress inhibits the growth of multicellular tumour spheroids. *Nature Biotechnology* 1997; **15**:778–783.
40. Stohrer M, Boucher Y, Stangassinger M, Jain RK. Oncotic pressure in solid tumors is elevated. *Cancer Research* 2000; **60**:4251–4255.
41. Bearer EL, Lowengrub JS, Frieboes HB, Chuang YL, Jin F, Wise SM, Ferrari M, Agus DB, Cristini V. Multiparameter computational modeling of tumor invasion. *Cancer Research* 2009; **69**(10):4493–4501.
42. Frieboes HB, Jim F, Chuang Y-L, Wise SM, Lowengrub JS, Cristini V. Three-dimensional multispecies nonlinear tumor growth—II: tumor invasion and angiogenesis. *Journal of Theoretical Biology* 2010; **264**:1254–1278.
43. Frieboes HB, Lowengrub JS, Wise S, Zheng X, Macklin P, Bearer EL, Cristini V. Computer simulation of glioma growth and morphology. *NeuroImage* 2007; **37**(S1):S59–S70.

DOI: 10.1002/cnm

44. Wise SM, Lowengrub JS, Frieboes HB, Cristini V. Three-dimensional diffuse-interface simulation of multispecies tumor growth—I. Model and numerical method. *Journal of Theoretical Biology* 2008; **253**(3):523–543.
45. Wise SM, Lowengrub JS, Cristini V. An adaptive multigrid algorithm for simulating solid tumor growth using mixture models. *Mathematical and Computer Modelling* 2011; **53**:1–20.
46. Cristini V, Li X, Lowengrub JS, Wise S. Nonlinear simulations of solid tumor growth using a mixture model: invasion and branching. *Journal of Mathematical Biology* 2009; **58**:723–763.
47. Oden JT, Hawkins A, Prudhomme S. General diffuse-interface theories and an approach to predictive tumor growth modeling. *Mathematical Models and Methods in Applied Sciences* 2010; **20**(3):477–517.
48. Coleman BD, Noll W. The thermodynamics of elastic materials with heat conduction and viscosity. *Archive for Rational Mechanics and Analysis* 1963; **13**:167–178.
49. Gurtin ME. Generalized Ginzburg–Landau and Cahn–Hilliard equations based on a microforce balance. *Physica D* 1996; **92**:178–192.
50. Groot SR, Mazur P. *Non-equilibrium Thermodynamics*. Dover: New York, 1984. Published originally by North-Holland Publishing Co, Amsterdam, 1962.
51. van der Zee KG, Oden JT, Hawkins-Daarud AJ, Prudhomme S. A four-species diffuse-interface tumor-growth model of gradient-flow type. In preparation.
52. Eyre DJ. Unconditionally gradient stable time marching the Cahn–Hilliard equation. In *Computational and Mathematical Models of Microstructural Evolution, volume 529 of Materials Research Society Symposium Proceedings*, Bullard JW, Chen L-Q, Kalia RK, Stoneham AM (eds). Materials Research Society: Warrendale, PA, 1998; 39–46.
53. Wise SM, Wang C, Lowengrub JS. An energy-stable and convergent finite-difference scheme for the phase field crystal equation. *SIAM Journal on Numerical Analysis* 2009; **47**(3):2269–2288.
54. Wise SM. Unconditionally stable finite difference, nonlinear multigrid simulation of the Cahn–Hilliard–Hele–Shaw system of equations. *Journal of Scientific Computing* 2010; **44**:38–68.
55. Zienkiewicz OC, Zhu JZ. The superconvergent patch recovery and a posteriori error estimates. Part 1: the recovery technique. *International Journal for Numerical Methods in Engineering* 1992; **33**(7):1331–1364.
56. Zienkiewicz OC, Zhu JZ. The superconvergent patch recovery and a posteriori error estimates. Part 2: error estimates and adaptivity. *International Journal for Numerical Methods in Engineering* 1992; **33**(7):1365–1382.

DOI: 10.1002/cnm